Taylor & Francis
Taylor & Francis Group

Check for updates

The effect of cell wall material strain and strain-rate hardening behaviour on the dynamic crush response of an aluminium multi-layered corrugated core

Mustafa Güden and İlker Canbaz

Dynamic Testing and Modeling Laboratory, Department of Mechanical Engineering, Izmir Institute of Technology, Gülbahçe Köyü, Urla, Izmir, Turkey

ABSTRACT

The effect of the parameters of the Johnson and Cook material model on the direct impact crushing behaviour of a layered 1050 H14 aluminium corrugated structure was investigated numerically in LS-DYNA at quasi-static ($0.0048\,\mathrm{m\,s^{-1}}$) and dynamic (20, 60, 150 and $250\,\mathrm{m\,s^{-1}}$) velocities. Numerical and experimental direct impact tests were performed by lunching a striker bar onto corrugated samples attached to the end of the incident bar of a Split Hopkinson Pressure Bar set-up. The numerical impact-end stress-time and velocity-time curves were further compared with those of rigid-perfectly-plastic-locking (r-p-p-l) model. Numerical and r-p-p-l model impact-end stress analysis revealed a shock mode at 150 and $250\,\mathrm{m\,s^{-1}}$, transition mode at $60\,\mathrm{m\,s^{-1}}$ and quasi-static homogenous mode at $20\,\mathrm{m\,s^{-1}}$. The increase of velocity from quasi-static to $20\,\mathrm{m\,s^{-1}}$ increased the numerical distal-end initial peak-stress, while it almost stayed constant between 20 and $250\,\mathrm{m\,s^{-1}}$ for all material models. The increased distal-end initial peak-stress of strain rate insensitive models from quasi-static to $20\,\mathrm{m\ s^{-1}}$ confirmed the effect of micro-inertia. The numerical models further indicated a negligible effect of used material models on the impact-end stress of investigated structure. Finally, the contribution of strain rate to the distal-end initial peak-stress of cellular structures made of low strain rate sensitive Al alloys was shown to be relatively low as compared with that of strain hardening and micro-inertia, but it might be substantial for the structures constructed using relatively high strain rate sensitive alloys.

1. Introduction

The strain rate sensitivity of metallic cellular structures may be in part or in combination due to compressed air in between crushed/bent/folded cells, the strain rate sensitivity of cell wall material, the micro-inertia of cell wall bending and inertia/shock formation [1]. Relatively low stress rise due to compressed air was reported for a closed-cell Al foam [2], but it might be substantial for very low density Al foams [3]. The strain rate sensitivity of cell wall material increases the crushing stress of metallic cellular structures at increasing impact velocities [4,5]. Similarly, the micro-inertia referred to as the delay of overall cell wall buckling increases cell wall buckling loads at increasing velocities [6,7]. The structures exhibiting steeply declining quasi-static load–displacement curve following an initial peak load (Type II) have shown to be more sensitive to impact velocities than the structures exhibiting a relatively flat-topped quasi-static load–displacement curves (Type I) [7]. The micro-inertia was previously shown for square thin-walled Al extrusions [8], closed-cell aluminium foams (from $3.33 \times 10^{-5}\ \mathrm{s^{-1}}$ to $1.6 \times 10^{-1}\ \mathrm{s^{-1}}$) [9], aluminium honeycombs [10], PVC foams and end-grain balsa wood (from $10^{-4}\ \mathrm{s^{-1}}$ to $4 \times 10^{3}\ \mathrm{s^{-1}}$) [11]. In two-phase cell wall buckling/bending (the plastic compression of walls and the rotations of plastic hinges), the micro-inertia was reported

dominant in the first phase and the strain rate sensitivity in the second phase [6], but both were equally effective in the deformation of Type II structures [12]. The shock mode of deformation however appears above a critical velocity with an indication of higher impact-end (impacted end) stress than distal-end (rear end) stress [13,14]. The difference between impact-end and distal-end stress increases as impact velocity increases above the critical velocity for shock formation. The densification strain was also shown to increase with increasing velocity [12,14–16]. The shock mode of deformation was shown in wood [17,18], urethane foam [19], open and closed cell aluminium foams [2,20–26], aluminium honeycomb [14] and multilayer corrugated structures [27].

Not only the crushing stress values but also the formation and progression of crush bands are altered with shock deformation mode. The initial cell wall collapse starts at the weakest layer and progresses non-sequentially in quasi-static mode, while the initial cell collapse starts at the impact end and progresses sequentially in a planner manner in shock deformation mode [13,28]. Agreements between the calculated and experimentally determined critical velocities for shock formation were previously reported for closed-cell Al foams [13,28]. In another study, open-cell 6061 Al foam samples impacted at $60\,\mathrm{m\ s^{-1}}$ or above showed shock deformation, while the samples impacted below $40\,\mathrm{m\ s^{-1}}$

CONTACT Mustafa Güden ✉ mustafaguden@iyte.edu.tr

exhibited a crushing mode very similar with the specimens tested at quasi-static velocity [12]. Apart from these, three deformation modes were shown for Al foams [29]: a quasi-static homogeneous mode in which the distal-end and impact-end stresses were equal at $16\,\mathrm{m\,s^{-1}}$, a transition mode at an intermediate velocity of $63\,\mathrm{m\,s^{-1}}$ and a shock deformation mode at $113\,\mathrm{m\,s^{-1}}$.

The velocity-dependent deformation behaviour of closed and open-cell Al foams, Al honeycombs and single- and double-layer Al corrugated cores were previously determined experimentally and numerically [2,14,16,20,24–26, 28,30–33]. The effect of strain rate on the out-of-plane plateau stress of an Al honeycomb using the Cowper–Symonds model with various strain rate hardening parameters was investigated numerically up to $200\,\mathrm{m\,s^{-1}}$ and experimentally up to $20\,\mathrm{m\,s^{-1}}$ [34,35]. It was shown that the plateau stress rise due to the strain rate sensitivity of cell wall material was only effective until about very low velocities ($\sim 10\,\mathrm{m\,s^{-1}}$), while inertial effects were dominant at high velocities. However, the effect of strain rate on the distal-end initial peak-stress and material flow stress model on the shock stresses of cellular structures have not been extensively investigated yet. Present study is therefore aimed to determine numerically the effect of strain rate and material flow stress model on the distal-end and impact-end crushing stresses of a layered 1050 H14 aluminium corrugated sandwich structure. The present study focuses on the distal-end initial peak-stress rather than plateau stress since it is the highest stress (before densification) that a structure experiences when it is protected against impact by a cellular structure. And, the results of present study may also be applied to cellular structures made of similar Al alloys. The investigated core was made of multilayer corrugated layers (fins) and was previously shown to display repeatable load-displacement responses [27,36,37]. On the other side, the dispersion of the strength of aluminium closed-cell foams widely used in dynamic crushing studies is comparably high, $\sim 20\%$ [2]. Partly because of this, the opposite results of the strain rate sensitivity of aluminium closed-cell foams were found in the literature [38]. As the investigated multi-layer corrugated structure displays repeatable responses to mechanical forces, it is also possible to construct 3D full models in order to monitor velocity and strain histories of each layer during the course of deformation. In addition, the corrugated core layers were in zig-zag form to facilitate fluid flow and thermal conduction. The corrugated sandwich structure forms a closed-loop system for a coolant to circulate within each layer when interlayer sheets are placed between each layer [39]. One of the potential applications is in the constructions of ammunition store walls. In this application, the sandwich absorbs the blast energy through the deformation of corrugated layers and the structure at the same time may supply coolant to extinguish any fire. Four different sets of material model parameters were investigated and 3D full geometric models of multi-layered structure were developed in the explicit finite element code of LS-DYNA. Geometrically imperfect layers were included in the geometrical models in order to validate the experimental

quasi-static stress–strain behaviour and to investigate their effects on the distal-end and impact-end stresses. The quasi-static compression geometrical model was implemented at $0.0048\,\mathrm{m\,s^{-1}}$ and the direct impact (stationary or forward impact) numerical test models at 20, 60, 150 and $250\,\mathrm{m\,s^{-1}}$.

2. Material and material models

The investigated multi-layered sandwich core was made of 1050 H14 Al trapezoidal zig-zag corrugated layers (fins) as shown in Figure 1(a). The structure was constructed using 15 zig-zag fin layers (see the inset of Figure 1(a)) brazed with 0/90 layer configuration and 1 mm-thick 1050 H14 Al face sheets (shown by arrows in Figure 1(a)). The height, width, length and thickness of a fin are sequentially 3.20, 1.6, 2.4 and 0.170 mm (Figure 1(b)). The details of the corrugated core processing are given elsewhere [27].

The quasi-static compression tests ($0.0048\,\mathrm{m\,s^{-1}}$) were performed using 40 mm diameter samples and the direct impact tests using 19.40 mm diameter samples. Essentially, 19.40 mm and 40 mm samples showed the same quasi-static stress–strain behaviour, while larger diameter sample was selected in order to observe layer crushing clearly. The test samples had the density of $326\,\mathrm{kg\,m^{-3}}$ without face sheets. The corrugated sandwich plate contained typical fin wall imperfections induced during brazing. The fin walls were slightly bent after brazing as shown in the inset of Figure 2(a). In addition, the fin walls at the outer surface of cylindrical test samples were significantly bent after cutting as seen in the inset of Figure 2(b). The fin walls were also thicker at the fin contact points which was attributed to the filler accumulation at these sites. The bent-walls after brazing and cutting were simulated by using bent-wall-fin-geometry model and inserting two imperfect fin layers to the model sample, respectively.

The initial modelling studies were on the determination of a representative numeric geometrical model for the experimental quasi-static and dynamic stress-strain behaviour of corrugated multi-layered structure. Once the representative numerical model geometry was determined, then the direct impact test models were implemented. The 3D quasi-static and dynamic test sample models were constructed using three different fin geometries. These are the perfect, imperfect and double imperfect fins as shown in Figure 3(a–c), respectively. In the imperfect and double imperfect fin models, a bent type of imperfection, 1.62 mm in radius, is introduced to the one and two-wall of the fins, respectively (Figure 3(b) and (c)). The model constructed using perfect unit fin geometry is coded as perfect geometry model (Figure 3(a)) and the model constructed using imperfect unit fin geometry is coded as imperfect geometry model (Figure 3(b)). In the two-layer imperfect geometry model, the 2nd and 10th layers from top to bottom (marked with arrows in Figure 3(c)) were constructed with double imperfect unit fin geometry. The perfect geometry model, imperfect geometry model and two-layer imperfect geometry model contained 125,906, 150,871 and 154,153 shell elements, respectively. The fins in the numerical sample model
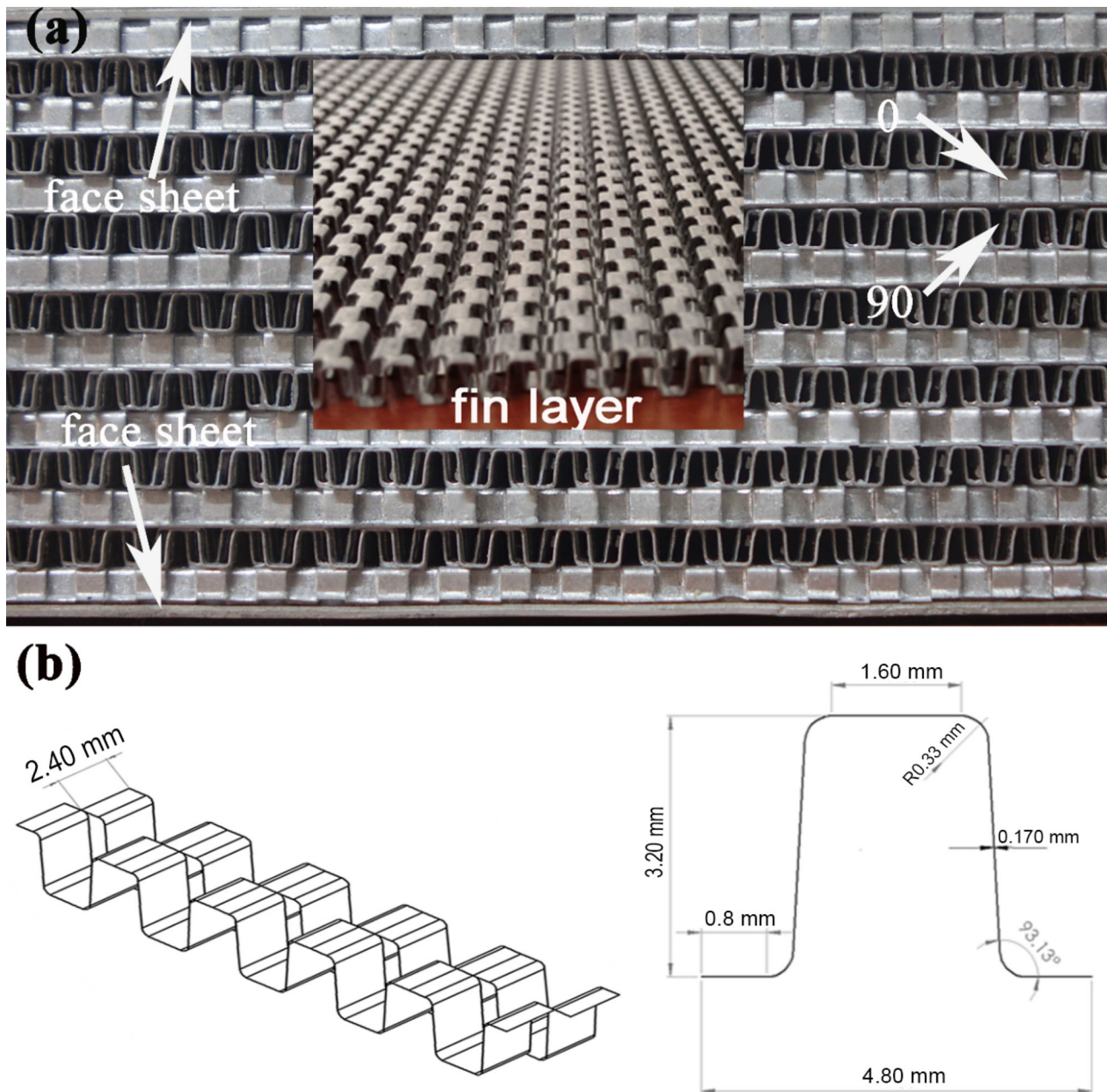
Figure 1. (a) The multi-layered sandwich plate cross-section and fin layer and (b) fin geometrical sizes.

had the same geometrical properties with the fins in the test sample. As the layered corrugated sandwich was formed by brazing the fin layers in a furnace at 600 °C (10 min) by the producer using a 4343 Al filler with ∼7 wt% of the panel, the thickness of the fin walls in the numerical sample model increased from 0.170 to 0.187 mm in order to account the filler material weight in the brazing process (7 wt% – corresponding to 0.017 mm thickness increase).

3. Quasi-static and dynamic tests and models

The used quasi-static compression numerical test model is shown in Figure 4. The compression bottom and top test platens of universal Shimadzu testing machine were modelled with *MAT_RIGID, Material type 20. The modulus of elasticity (E) of steel test platens was 210 GPa and the

Poisson's ratio 0.3. The bottom test platen was constructed using 19,200 solid elements and fully constrained in all directions. The top test platen was modelled using the same number of solid elements and moved only through the axial-direction with a velocity the same as the compression test velocity, $0.0048 \, \text{m s}^{-1}$.

BOUNDARY_PRESCRIBED_MOTION_RIGID card was used to give constant z-direction velocity to the top cross-head. The total time of quasi-static simulation was defined with CONTROL_TERMINATION card. Since the total CPU time for quasi-static test solutions are relatively long, the mass scaling was applied in the quasi static simulations. The mass was added or removed from the elements. In order to determine the mass scaling factor, the simulation was initially run without mass scaling and the determined time step was multiplied by 10, 100 and 1000. It was found
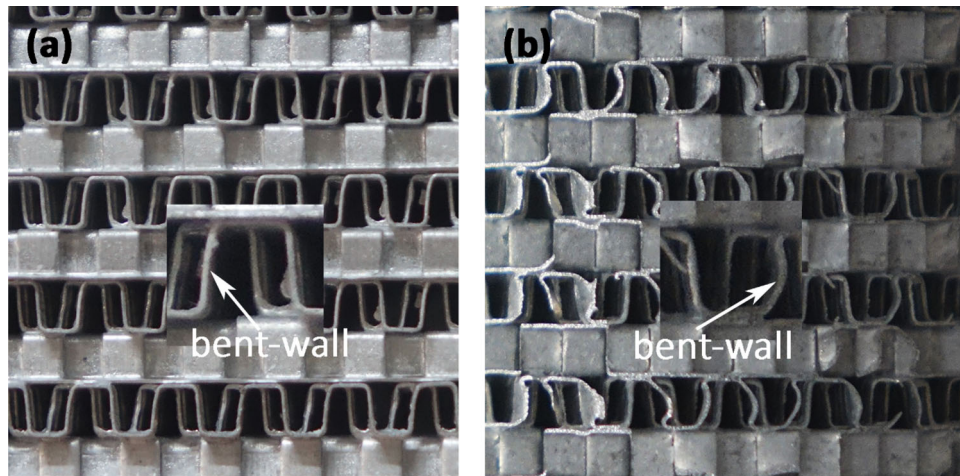
Figure 2. The pictures of the (a) as-received sandwich core surface fins and (b) the machined surface fins of a cylindrical test sample with bent-wall shown by arrow.
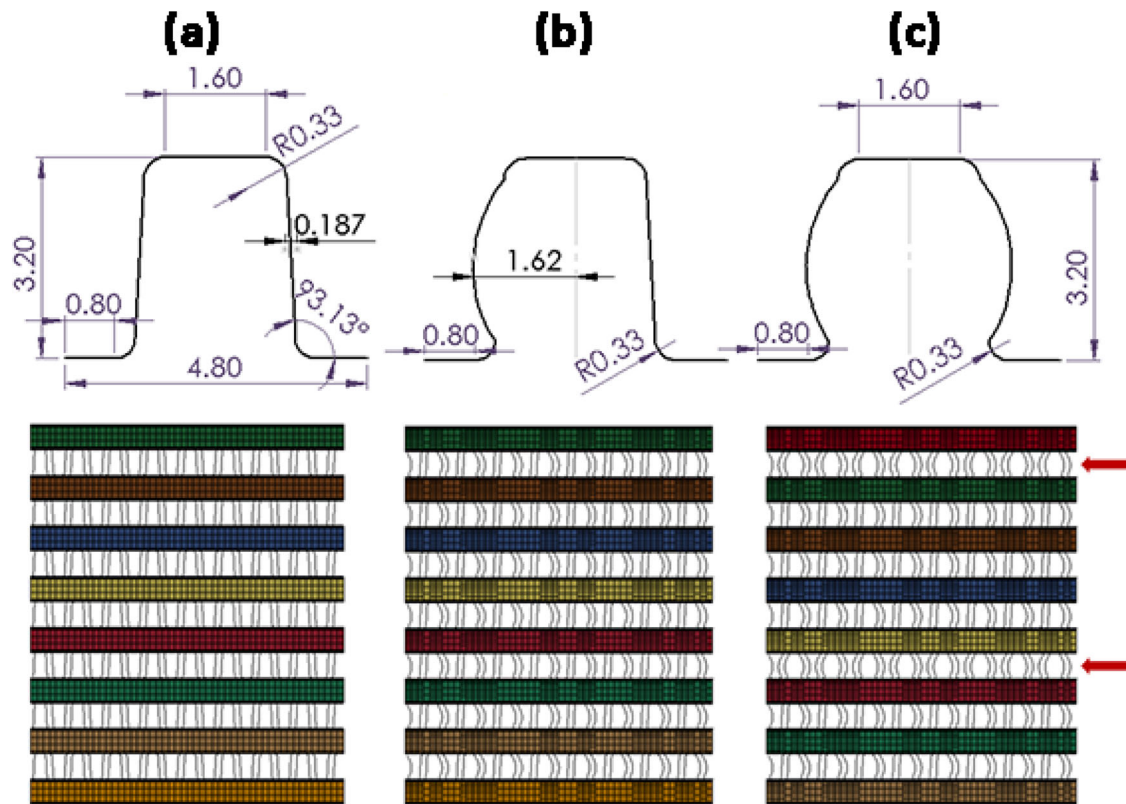

Figure 3. (a) Perfect unit fin and the perfect geometry model, (b) imperfect unit fin and the imperfect geometry model and (c) double imperfect unit fin and the two-layer imperfect geometry model.

numerically that the kinetic energy change was substantially lower than the internal energy change when the mass scaling factor was 1000. The termination time was taken as 10,000 milliseconds. The mass scaling method was implemented by using CONTROL_TIMESTEP card (time step size for mass scaled solutions, DT2MS was 0.0198). The contacts between steel compression plate and sample were determined with AUTOMATIC_SURFACE_TO_SURFACE. The static and dynamic friction coefficients were 0.3 and 0.2, respectively. These friction coefficients were previously implemented in modelling the same corrugated sample and resulted in comparatively similar stress–strain curves with

those of quasi-static and dynamic tests [40,41]. The contacts between each layer of corrugated sample were defined by CONTACT_ERODING_SINGLE_SURFACE card.

The direct impact tests were performed previously [41] at 22, 40, 60, 80 and 90 m s^{-1} in a modified Split Hopkinson Pressure Bar (SHPB) testing apparatus as shown in Figure 5. In these tests, the corrugated sample was attached to the end of the incident bar and 20 cm-long Al striker bar with an initial velocity impinged the sample (Figure 5). During the tests, the distal-end stress of the impacted corrugated sample was measured using two full-bridge strain-gage circuits on the incident bar: one was 300 mm and other
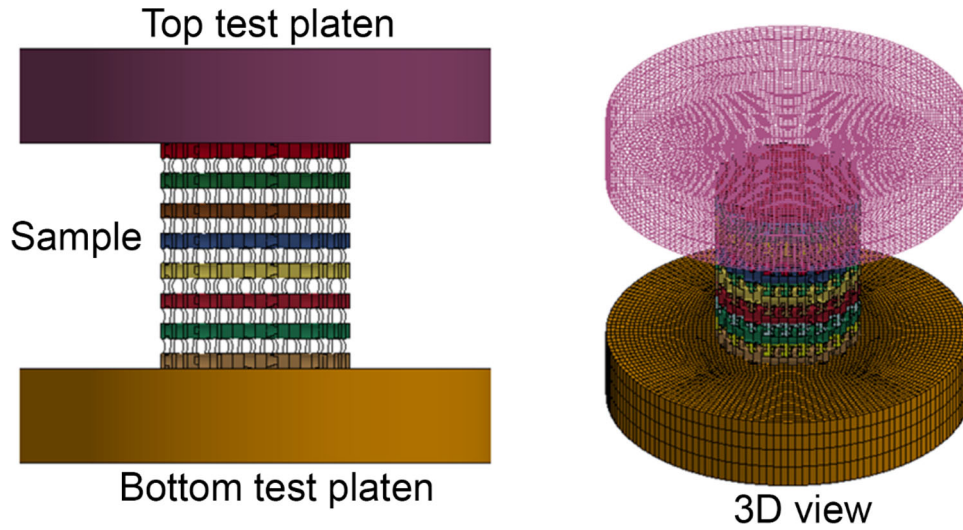
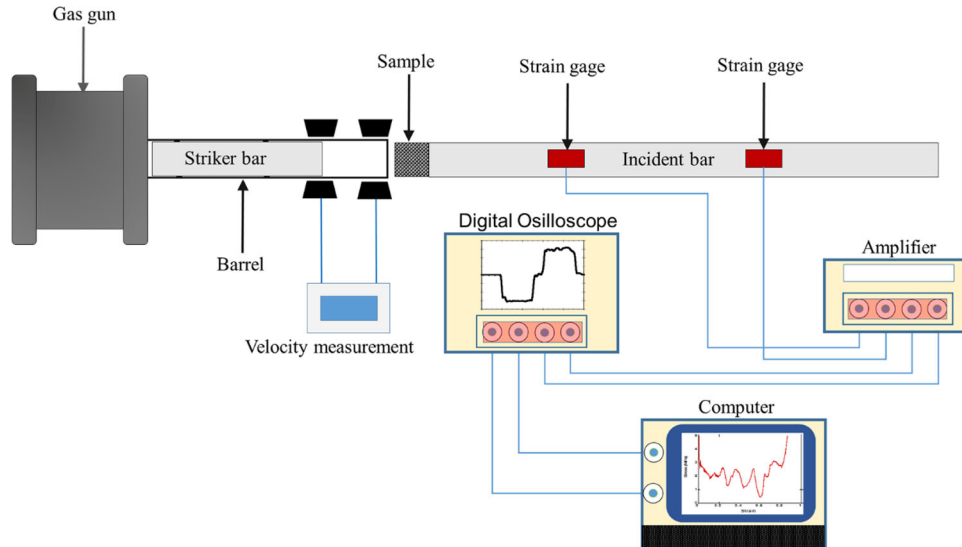**Figure 4.** Front and 3 D view of quasi-static compression numeric model.

Figure 5. The schematic drawing of direct impact test in modified SHPB set-up.

1110 mm away from impact-end (Figure 5). The striker bar velocity was measured just before the impact using two laser diodes placed at the exit of gas gun barrel. The striker bar and the test sample had the same diameter, 19.40 mm, with the incident bar. The 19.40 mm-diameter test samples were extracted from a sandwich plate by means of an electro-discharge machine.

The full direct impact test model and the sample bar interfaces are shown in Figure 6. The diameter of the model test sample is 19.4 mm and the length is 48 mm (composing of 15 layers). Inconel 718 incident bar and 20 cm-long Al striker bar were modelled using MAT_ELASTIC material model (material type 01) and 15 mm-size 28,980 and 4800 solid elements, respectively. The density, elastic modulus and Poisson's ratio of Inconel and Al were sequentially taken as $7850\,\mathrm{kg\,m^{-3}}$, 207 GPa, 0.33 and $2700\,\mathrm{kg\,m^{-3}}$, 70 GPa and 0.33.

The contacts between bars and sample were defined by the AUTOMATIC_SURFACE_TO_SURFACE contact algorithm. The total time of dynamic simulation was defined by the CONTROL_TERMINATION card with a termination time of 3 milliseconds and the initial velocity by the INITIAL_VELOCITY_GENERATION card.

The corrugated test sample was modelled using the Johnson and Cook flow stress material model (*MAT_SIMPLIFIED_JOHNSON_COOK, Material type 98) with different sets of parameters

$$\sigma_e = \left[A + B\varepsilon_P^n\right]\left[1 + c\,\mathrm{In}\dot{\varepsilon}_P^*\right] \tag{1}$$

where, σ_e is the equivalent stress, A and B are the constants, ε_P is the equivalent plastic strain, n is the strain hardening parameter and c is the strain rate sensitivity parameter. In the same equation, $\dot{\varepsilon}_P^*$ denotes the strain rate ratio calculated as $\frac{\dot{\varepsilon}_P}{\dot{\varepsilon}_0}$, where $\dot{\varepsilon}_P$ is the equivalent plastic strain rate and $\dot{\varepsilon}_0$ is the reference equivalent plastic strain rate. The effect of temperature was not taken into account in present study. The material model parameters of 1050 H14 Al were determined previously and given as: $A = 102\,\mathrm{MPa}$, $B = 97.25\,\mathrm{MPa}$, $n = 0.18$ and $\dot{\varepsilon}_0 = 10^{-3}\,\mathrm{s^{-1}}$ [36].
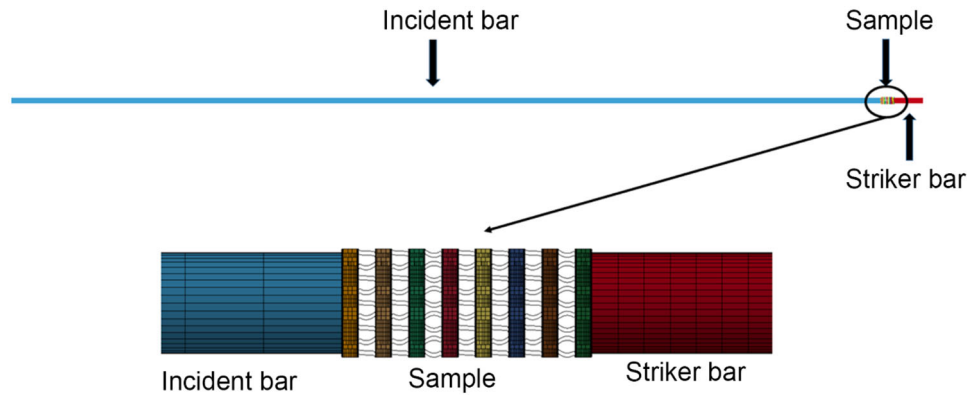
Figure 6. The direct impact SHPB test model and interfaces between the bars and sample.

Table 1. The sets of material model parameters used in the numerical simulations.

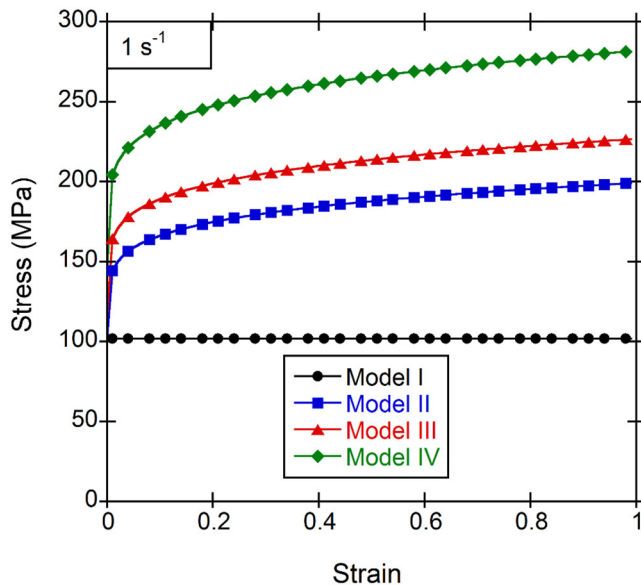| Designation	A (MPa)	B (MPa)	n	c	Model effects
MM-I	102	0	0	0	Perfect plastic
MM-II	102	97.25	0.18	0	Strain hardening
MM-III	102	97.25	0.18	0.02	Strain and strain rate hardening with low strain rate sensitivity
MM-IV	102	97.25	0.18	0.06	Strain and strain rate hardening with high strain rate sensitivity

Figure 7. The stress–strain curves of MM-I, MM-II, MM-III and MM-IV at $1\,s^{-1}$.

Figure 8. The quasi-static stress–strain curves of the test and perfect, imperfect and two-layer imperfect geometry model using MM-II.

Four different sets of parameters were used in the numerical simulations as tabulated in Table 1. These were (1) the perfect plastic: $A = 102\,MPa$, $B = 0\,MPa$, $n = 0$ and $c = 0$, (2) the strain hardening: $A = 102\,MPa$, $B = 97.25\,MPa$, $n = 0.18$ and $c = 0$, (3) the strain and strain rate hardening: $A = 102\,MPa$, $B = 97.25\,MPa$, $n = 0.18$ and $c = 0.02$ and (4) the strain and strain rate hardening with $c = 0.06$. These sets of material model parameters were coded as MM-I, MM-II, MM-III and MM-IV, respectively. The strain rate sensitivity of Al and its alloys are known to be relatively low. The rate sensitivity of heat-treated alloys was reported between 0.01 and 0.015, 1100 and 1060 alloys between 0.004 and 0.06 and pure Al between 0.07 and 0.9 [42]. Therefore, the selected rate sensitivity parameters are in accord with the experimentally determined strain rate sensitivities of similar alloys. The stress-strain curves of investigated corrugated core material parameter sets at $1\,s^{-1}$ are shown in Figure 7.
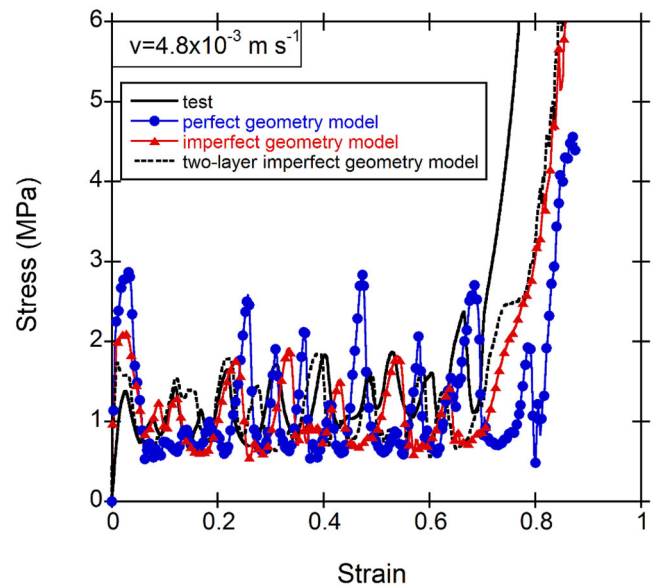
Shortly, MM-II was used to determine the effect of strain hardening, MM-III the effect of strain rate hardening and MM-IV the effect of increasing strain rate sensitivity parameter on the crushing behaviour.

4. Results and discussion

4.1. Effect of geometry model

The quasi-static stress–strain curves of the test, perfect, imperfect and two-layer imperfect geometry model using MM-II are shown in Figure 8. The perfect geometry model results in relatively higher initial and post initial peak-stresses than the test. It is noted in the same figure that the peak and valley-stresses and the densification strain of the test are better approached by the imperfect geometry model
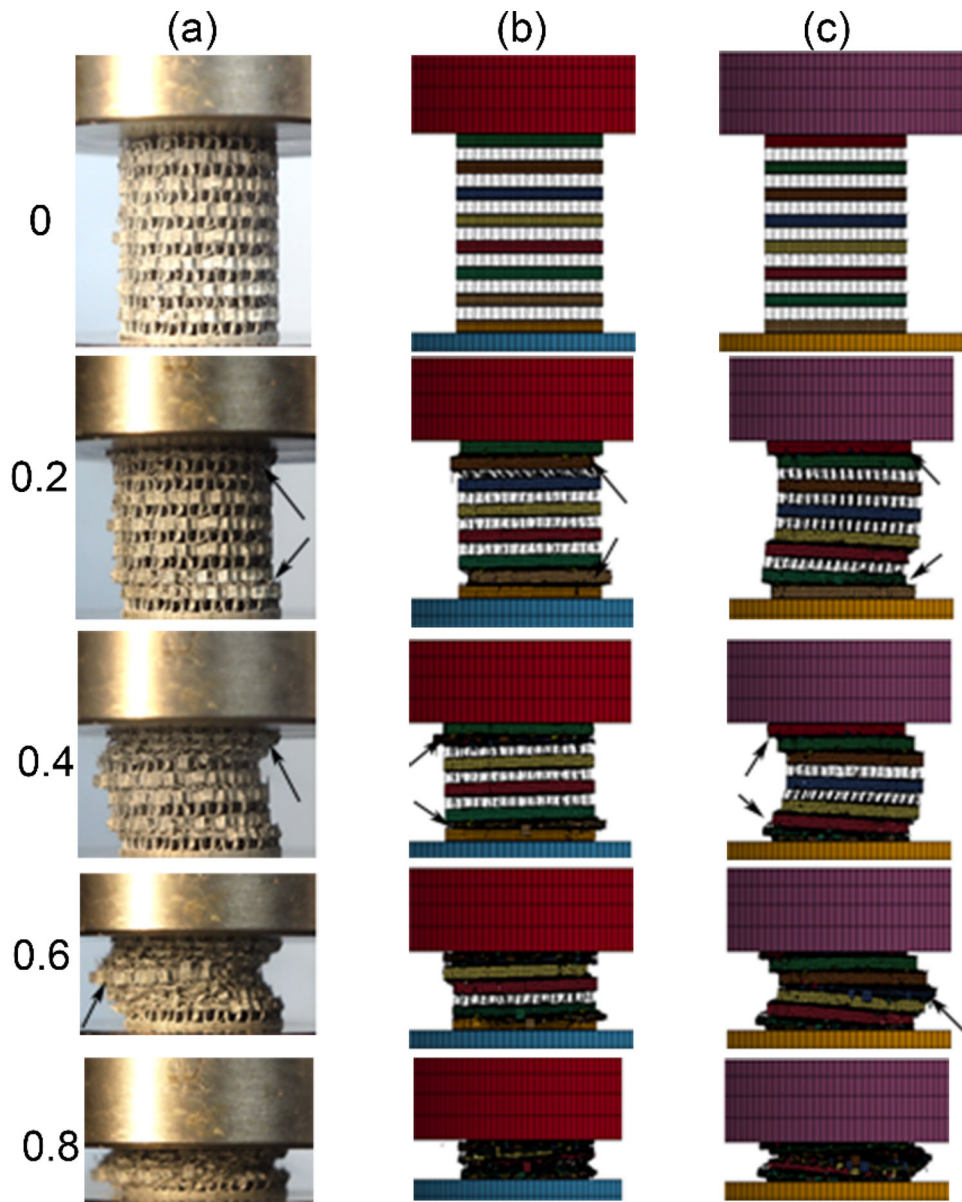
Figure 9. The quasi-static deformation pictures of (a) test, (b) imperfect geometry model and (c) two-layer imperfect geometry model at 0, 0.2, 0.4, 0.6 and 0.8 strain (numbers show strain).

and two-layer imperfect geometry model. The deformation pictures of the test, imperfect geometry model and two-layer imperfect geometry model at 0, 0.2, 0.4, 0.6 and 0.8 strain are shown sequentially in Figure 9(a–c). The initial layer crushing in the test starts at the bottom sections of the sample at 0.2 strain; then, the layer crushing continues at the upper layers as the strain increases (shown by arrows in Figure 9(a)). Mid-section layers crush at a later stage of the deformation and the layer crushing causes the shearing of mid-section layers, resulting in the bending of the test sample at 0.6 strain (shown by an arrow in Figure 9(a)). The layer crushing in the imperfect geometry model starts at the bottom and top layers as seen and marked by arrows in Figure 9(b). As similar with the test sample, the numerical mid-section layers crush at a later stage. The extent of specimen bending is noted to be significantly reduced in the imperfect geometry model. In the two-layer imperfect geometry model, the layer crushing however initiates at the 2nd and 10th layer

(imperfect layers-marked by arrows in Figure 9(c)). Later, the layer crushing switches to the top and bottom layers, followed by the crush of mid-section layers. The sample bending is also clearly seen in Figure 9(c), starting at ∼0.4 strain, almost the same as the test. The test deformation sequence and final deformed shape of test sample are concluded to be well approached by the two-layer imperfect geometry model. Further modelling efforts were therefore continued with the use of the two-layer imperfect geometry model and the imperfect geometry model was only used to determine the effect of imperfect layers on the crushing stress.

4.2. Effect of set of material model parameter

In previous experimental and numerical studies, the MM-II was shown to result in numerical stresses similar with the quasi-static compression tests, direct impact tests at 22, 40, 60, 80 and 90 m s^{-1} [41] and Taylor-like impact tests at 135,
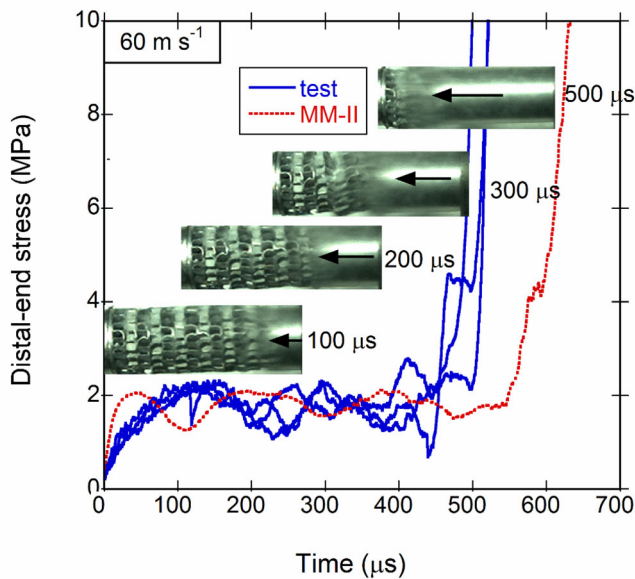
Figure 10. The direct impact distal-end stress–strain curves of the test and MM-II at 60 m s^{-1} (arrows show the impact end).

250 and 200 m s^{-1} [40]. Figure 10 shows the numerical direct impact distal-end stress–time curve of MM-II (two-layer imperfect model) together with three experimental distal-end stress–time curves at 60 m s^{-1}. As seen in the same figure, the model and test distal-end initial peak and post initial peak-stresses are very similar at 60 m s^{-1}, $\sim$ 2 MPa, while the model sample densifies at a longer time than the test sample. The layer crushing in the test starts at the impact-end layers and proceeds to the undeformed layers as the deformation time increases as depicted in the inset of Figure 10.

The quasi-static stress–strain curves of M-I, MM-II and MM-III are shown in Figure 11(a) together with that of a test. As seen in the same figure, the stress-strain curves of MM-II and MM-III are very similar because of relatively low strain rate involved in the quasi-static test, while MM-I shows relatively lower crushing stresses. Although it is not shown in Figure 11(a), MM-IV showed the same quasi-static stress–strain behaviour with MM-III. The lower crushing stresses of MM-I as compared with those of MM-II, MM-III and MM-IV are due to lack of strain hardening in MM-I. The strain hardening also decreases densification strain as seen in Figure 11(a). The initial peak-stress (marked in Figure 11(a)) is determined 1.27 MPa for MM-I and 1.74 MPa for MM-II, MM-III and MM-IV. The distal-end stress–time curves of MM-I, MM-II, MM-III and MM-IV at 20, 60 and 150 m s^{-1} are shown in Figure 11(b–d), respectively. As the velocity increases, the difference in the distal-end stresses between materials models increases. As is expected, MM-IV shows the highest and MM-I the lowest distal-end stresses. Shortly, both strain hardening and strain rate increase distal-end stresses at increasing velocities.

The impact-end stress–time curves of material models at 20, 60, 150 and 250 m s^{-1} are shown in Figure 12(a–d), respectively. The increase of velocity from quasi-static to 20 m s^{-1} increases the initial peak-stresses of all the sets of material model parameters as compared with quasi-static

peak-stress, but post-peak-stress values become very much similar with those of quasi-static after $\sim$500 μs. The impact-end stresses get much higher than that of quasi-static when the velocity increases to 60, 150 and 250 m s^{-1} and the impact-end stresses of all the sets of material model parameters get close to each other as seen in Figure 12(b–d). It is also noted in Figure 12(a–d) that the magnitude of stress oscillations increases with increasing velocity.

Figure 13(a–d) shows sequentially the distal-end nominal stress–strain curves of MM-I, MM-II, MM-III and MM-IV at increasing velocities. As seen in the same figure, the distal-end initial peak and post-peak-stresses of all the sets of material model parameters increase with the increase of velocity from quasi-static velocity to 20 m s^{-1}. Thereafter, the distal-end initial peak-stresses remain almost constant or increase slightly, while the post-peak-stresses increase with increasing velocity. The effect of the sets of material model parameters on the distal-end stresses is also seen in Figure 13(a–d). Both, the strain and strain rate hardening increase distal-end stresses including both initial peak and post-peak-stresses. Although, the distal-end stresses following the initial peak-stress at 20 m s^{-1} are very similar with those of quasi-static, the distal-end stresses at 60, 150 and 250 m s^{-1} are much higher than those at quasi-static velocity.

The deformation pictures of MM-II at 20, 60 and 150 m s^{-1} are shown in Figure 14(a–c), respectively. At all velocities, the initial layer crushing starts at the impact-end, while the layer crushing is non-sequential at 20 m s^{-1} (Figure 14(a)) and diffusive at 60 m s^{-1} (Figure 14(b)). The layer crushing however progresses sequentially from the impact-end to the distal-end at 150 m s^{-1}, showing a shock deformation mode (Figure 14(c)). The shock deformation mode was also detected at 250 m s^{-1}. As with the two-layer imperfect geometry model, the layer crushing in the imperfect geometry model started at the impact-end at all velocities.

4.3. Comparison with the rigid-perfectly-plastic-locking model and the simplified model of foam plateau stress

The variations of the distal-end initial peak-stress of MM-I, MM-II, MM-III and MIV with velocity are shown in Figure 15(a). The distal-end initial peak-stress increases with increasing velocity from quasi-static to 20 m s^{-1}. But after 20 m s^{-1}, the distal-end initial peak-stress remains almost constant. An average dynamic distal-end peak-stress was determined between 20 and 250 m s^{-1} for each set of material model parameters as seen in Figure 15(a). The dynamic distal-end average peak-stress is 1.67, 2.16, 2.45 and 2.91 MPa for MM-I, MM-II, MM-III and MM-IV, respectively. In the same figure, the distal-end initial peak-stress of the imperfect geometry model (MM-II) is also shown. The dynamic distal-end peak-stress of the imperfect geometry model is 2.35 MPa. On the other side, the quasi-static (0.0048 m s^{-1}) distal-end peak-stress is 1.27 for MM-I, 1.73 MPa for MM-II, MM-III and MM-IV and 2.1 MPa for the imperfect geometry model. The distal-end peak-stress increases 31.5%, 24.8%, 41.6% and 68.2% for MM-I, MM-II, MM-III and MM-IV at dynamic velocities, respectively.
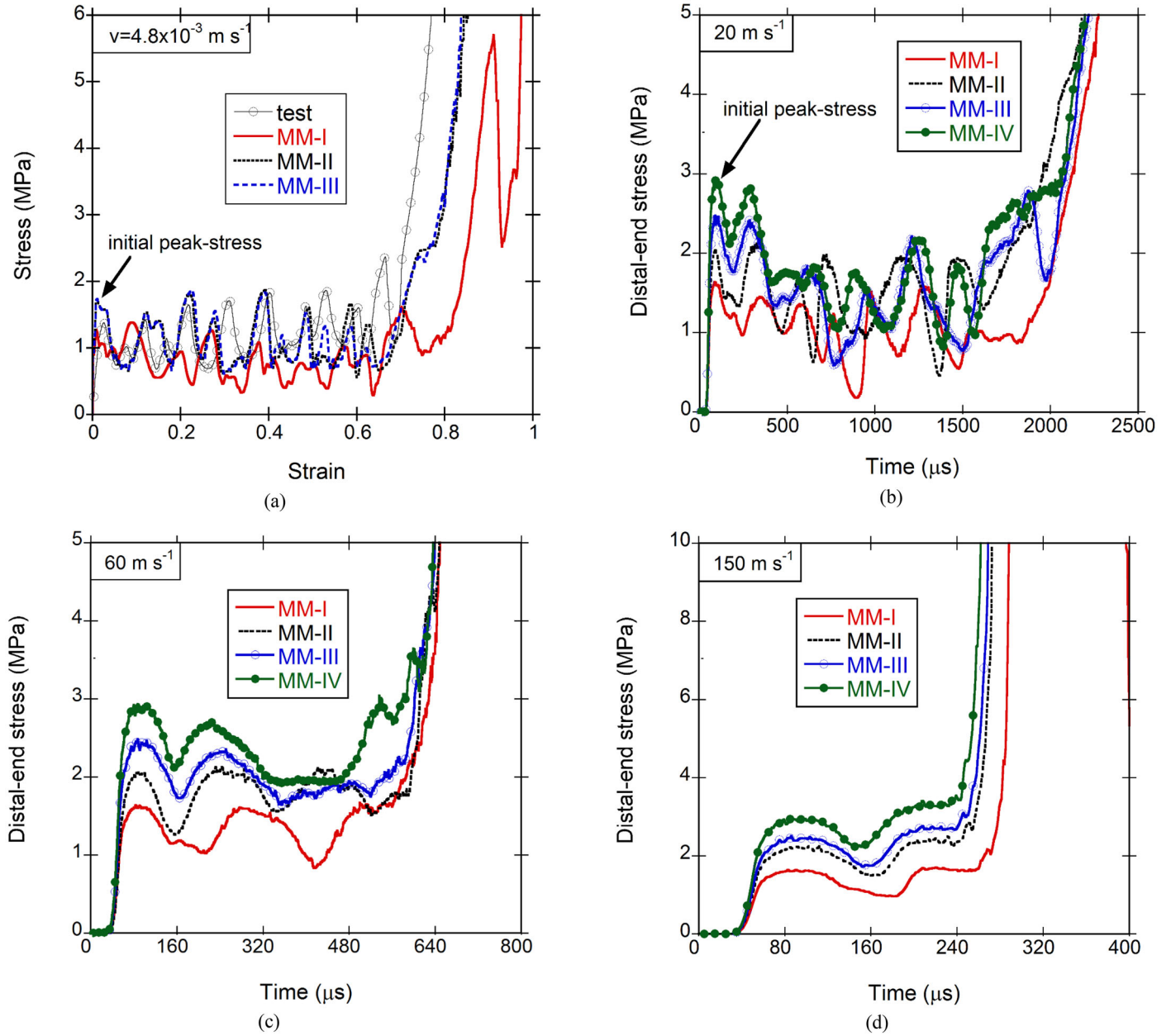
Figure 11. (a) The quasi-static stress–strain curve and the distal-end stress–time curves of samples with different material models at (b) 20, (c) 60 and (d) 150 m s^{-1}.

Using the distal-end average initial peak-stress of each material model as the plateau stress (σ_p), the impact-end stress (σ^*) and velocity (v) were calculated as function of time (t) using the rigid-perfectly-plastic-locking (r-p-p-l) model as [43]

$$\sigma^*(t) = \frac{\left(\frac{M}{A_o}\right)^2 \left(\sigma_p + \frac{\rho_o}{\varepsilon_d} v_o^2\right)}{\left(\frac{M}{A_o} + \frac{\rho_o u}{\varepsilon_d}\right)^2} \quad (2)$$

and

$$v(t) = \sqrt{\frac{\varepsilon_d}{\rho_o} \left[\frac{\left(\frac{M}{A_o}\right)^2 \left(\sigma_p + \frac{\rho_o}{\varepsilon_d} v_o^2\right)}{\left(\frac{M}{A_o} + \frac{\rho_o u}{\varepsilon_d}\right)^2} - \sigma_p \right]} \quad (3)$$

where M is the mass of Al striker, A_o is the cross-sectional area of sample, ρ_o is the density of sample, ε_d is the densification strain, u is the displacement and v_o is the velocity of striker. Following parameters were used the calculations: $\rho_o = 326$ kg m^{-3}, $\varepsilon_d = 0.72$ and the diameter of test sample $= 19.40$ mm. The results of the r-p-p-l model impact-end stress calculations of MM-II based on the distal-end average initial peak-stress are shown in Figure 12(a–d) for 20, 60, 150 and 250 m s^{-1}, respectively. Although the r-p-p-l model stress calculation show well agreement with the numerical impact-end stress at the initial times of impact at 20 m s^{-1} and 60 m s^{-1}, it over predicts the stresses at increasing times (Figure 12(a,b)). While, the r-p-p-l model stress calculation shows thoroughly well agreement with the numerical impact-end stresses at 150 and 250 m s^{-1} (Figure 12(c,d)). This also proves the existence of shock stress after 60 m s^{-1}
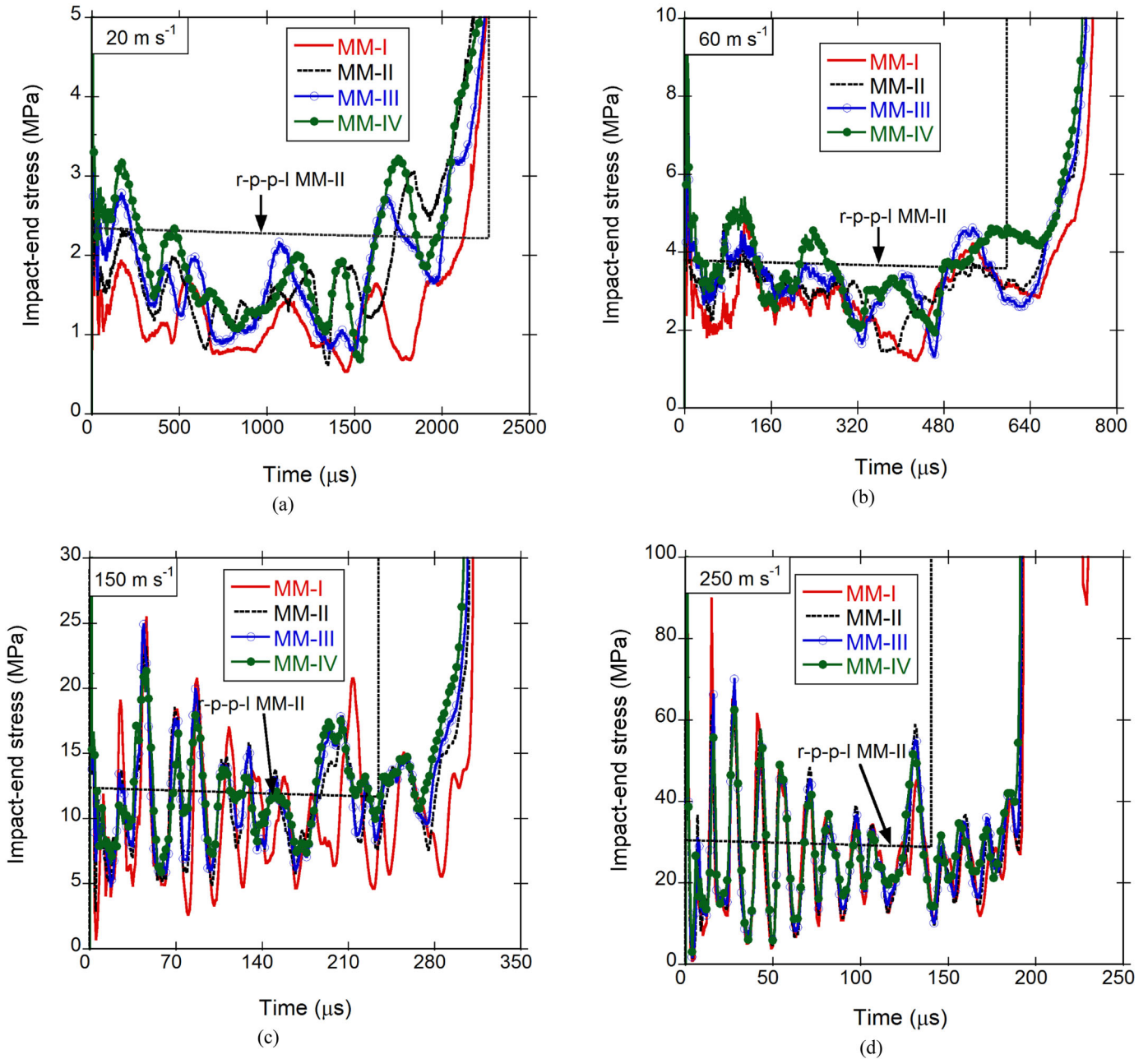
Figure 12. The impact-end stress–time curves of samples with different sets of material model parameters at (a) 20, (b) 60, (c) 150 and (d) 250 m s^{-1}.

since the r-p-p-l model predicts merely the shock stresses. The discrepancies between the densification strains and stresses of the r-p-p-l model and numerical model in the shock mode of deformation are ascribed to the fact that the r-p-p-l model is based on the quasi-static densification strain and plateau stress, while the densification strains and stresses in the model are determined by the deformation of the fin layers. By considering all internal energy was due to the loss of the kinetic energy, the following equation was proposed for the critical velocity (v_{cr}) for the shock formation [28]

$$v_{cr} = \sqrt{\frac{2\sigma_p \varepsilon_d}{\rho_o}} \qquad (4)$$

Taking $\sigma_p = 2.16$ MPa, $\rho_o = 326$ kg m^{-3} and $\varepsilon_d = 0.72$ gives a critical velocity of ~115 m s^{-1}. This calculated

critical velocity is also in accord with the numerically determined shock deformation mode at 150 and 250 m s^{-1}. Therefore, the r-p-p-l model in present study is only applicable at 150 and 250 m s^{-1} and it gives higher crushing stresses than the numerical model at relatively lower velocities. Figure 15(b) shows the impact-end stress and velocity–time curves of the imperfect geometry model (MM-II) and two-layer imperfect geometry model (MM-II) together with the stress and velocity–time curves of the r-p-p-l models at 250 m s^{-1}. The numbers at the peak-stresses in the same figure represent the completion of individual layer crushing. Since the two-layer imperfect model contains two double-wall-bent unit fin layers and all other layers are made of single-wall-bent unit fin layers and the imperfect geometry model are all made of single-wall-bent unit fin layers, Figure 15(b) also shows the effect of insertion
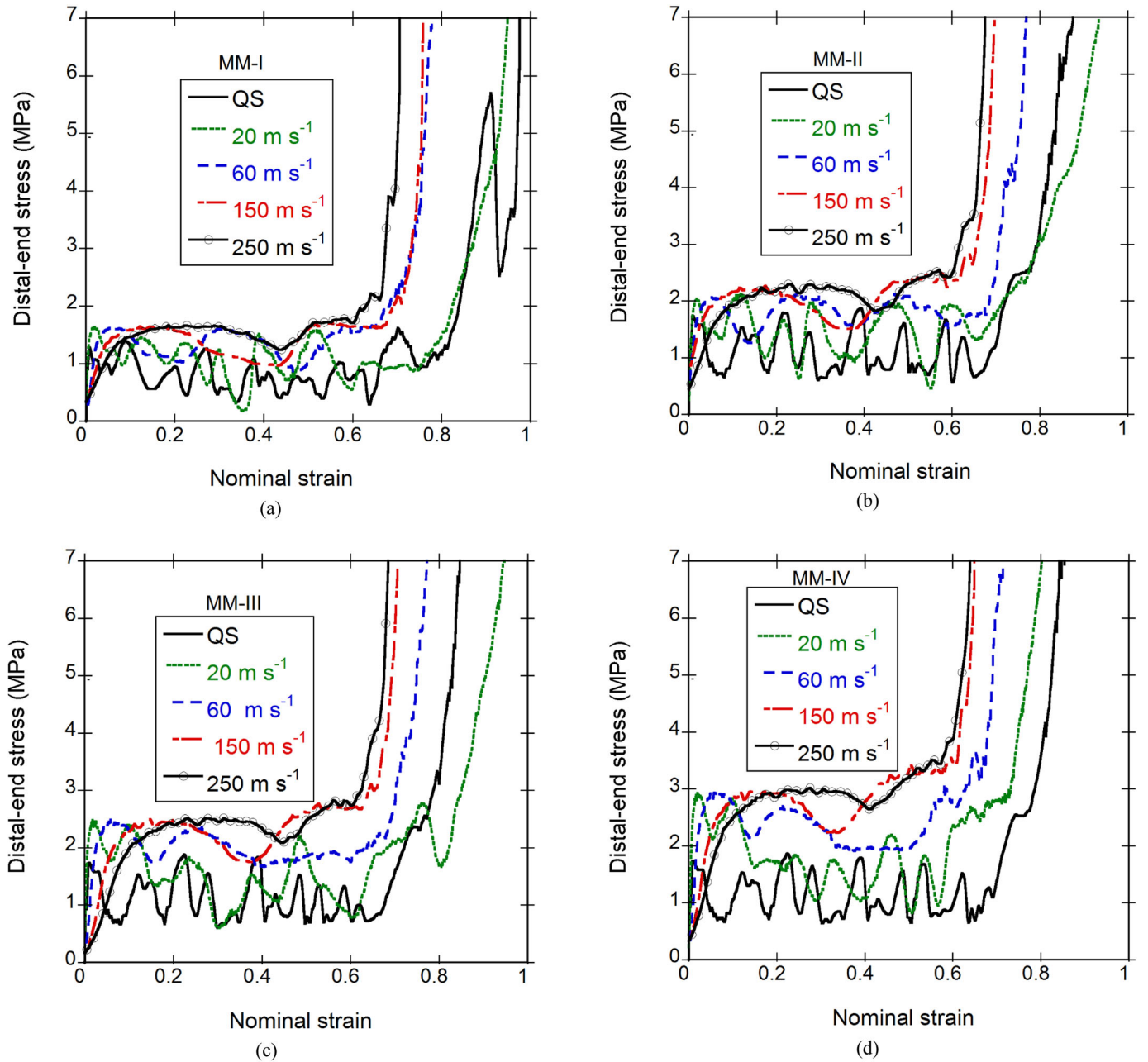
Figure 13. The distal end stress–nominal strain curves of samples at different velocities (a) MM-I, (b) MM-II, (c) MM-III and (d) MM-IV.

imperfect layers on the impact-end stresses. At the crushing of imperfect layers (2nd and 10th layer), the imperfect geometry model shows higher peak-stresses, while at the crushing of following layers (3rd and 11th layer), imperfect layer exhibits higher stresses. Apart from these, both geometry models show the same numerical and r-p-p-l model impact-end stresses and velocities and the same densification strains (0.72). Note that as the r-p-p-l model assumes a constant densification strain and excludes the elastic strains, it results in lower densification strains and higher velocities than the numerical model. The effect of imperfect layers on the impact-end stress is however somehow less pronounced in MM-I as compared with MM-II as seen in Figure 15(c). The peak-stress values of MM-II after the fifth layer decreases as compared with strain hardening MM-II. But, strain hardening has almost no effect on the valley-stresses,

densification strain and the r-p-p-l model stress and velocity values as seen in the same figure. There are also no significant effect of strain rate hardening models on the densification strain and the r-p-p-l model stress and velocity values as shown in Figure 15(d). The only effect of the strain rate hardening model is to decrease slightly the magnitude of stress oscillations by reducing the peak-stress values and increasing the valley-stress values.

The investigated corrugated structure may be considered as an Al open-cell foam with a plateau stress of [44]

$$\sigma_p = C_1 \sigma_y \left(\frac{\rho_o}{\rho_s}\right)^{3/2} \quad (5)$$

where, σ_y and ρ_s are the yield stress and the density of Al alloy and C_1 is a constant, ~ 0.3. By taking $\sigma_y = 102\,\text{MPa}$, $\rho_o = 326\,\text{kg m}^{-3}$ and $\rho_s = 2700\,\text{kg m}^{-3}$ and using Equation
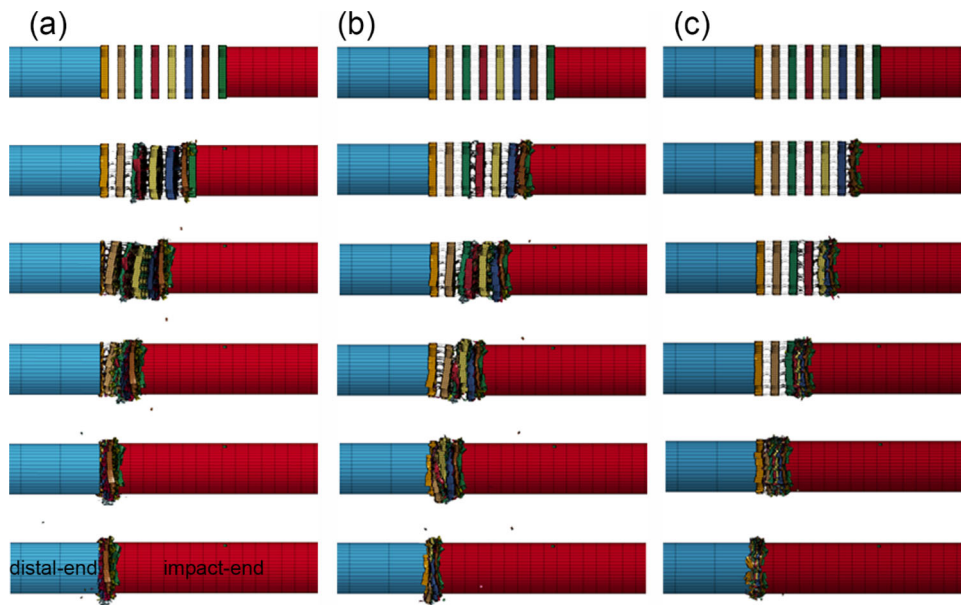
Figure 14. The deformation pictures of MM-II at (a) 20, (b) 60 and (c) 150 m s⁻¹.
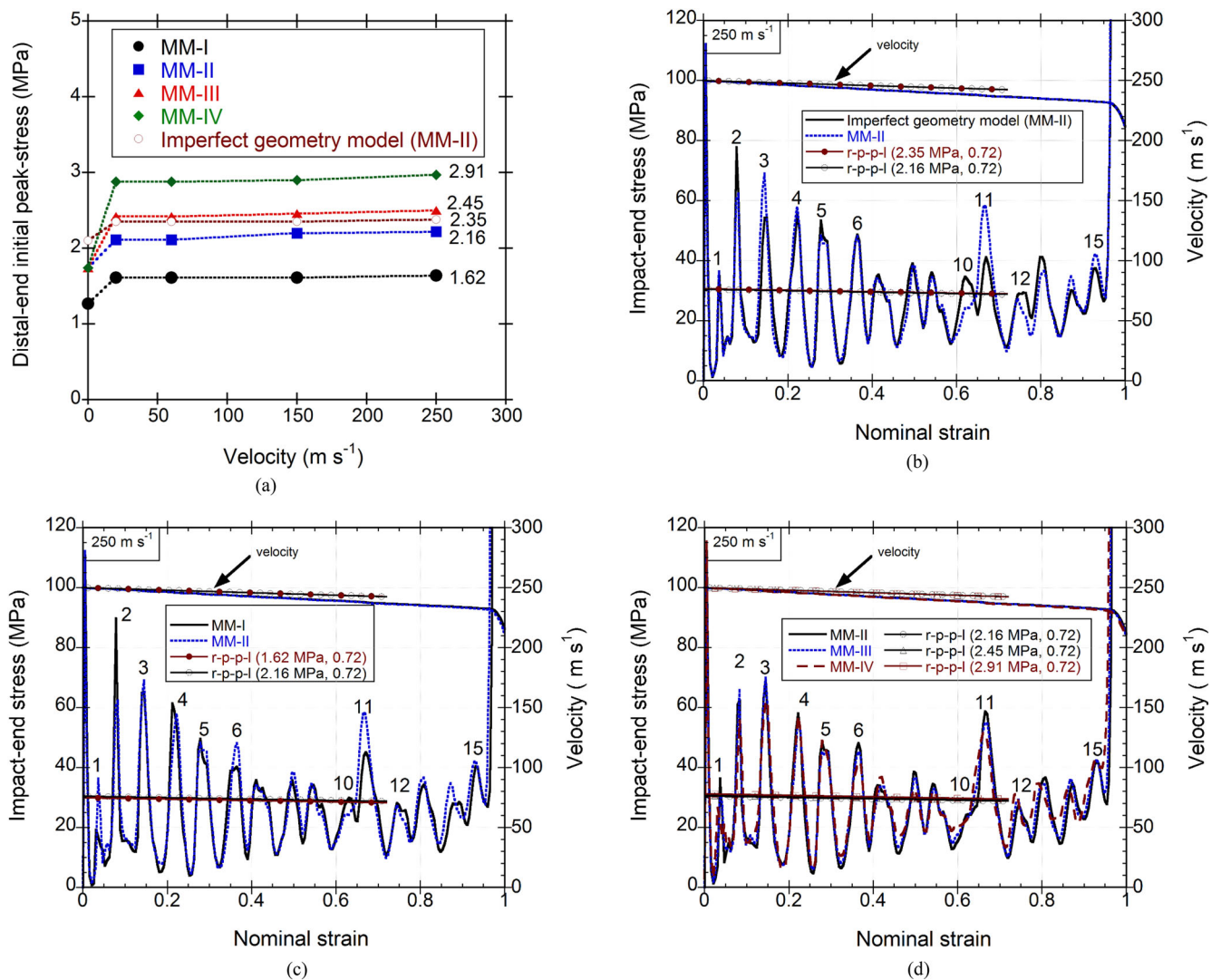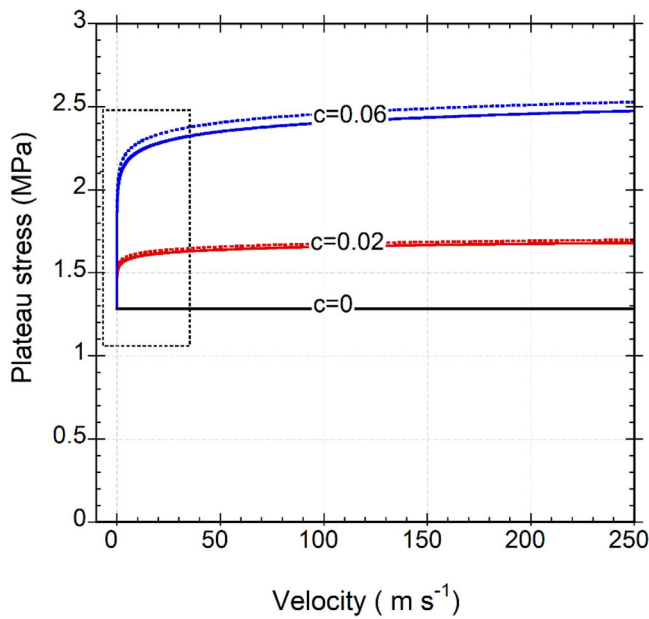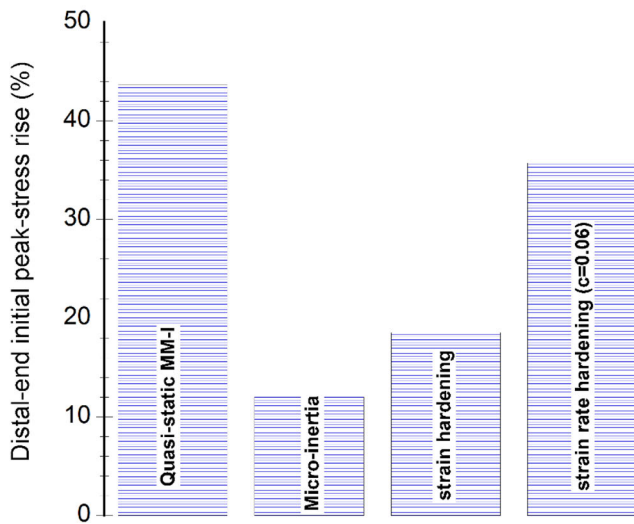

Figure 15. (a) the variation of distal-end stress with velocity and impact-end stress vs. nominal strain graphs of (b) the imperfect geometry model (MM-II) and the two-layer imperfect geometry model (MM-II), (c) MM-I and MM-II and (d) MM-II, MM-III and MM-IV at 250 m s⁻¹ together with the r-p-p-l model predictions.

(a)

(b)

Figure 16. The effect of velocity (strain rate) on the plateau stress based on Equation (5) and MM-I and (b) numerical relative contributions to distal-end peak-stress.

(5), the plateau stress was determined 1.28 MPa. This calculated plateau stress is comparable with the experimentally determined average initial peak-stress, 1.32 MPa (1.25–1.44 MPa) and average plateau stress, 1.02 MPa (0.95–1.1 MPa), at quasi-static strain rate.

It is known that, the average nominal strain rate underestimates the actual local strain rate. It was previously shown for an Al honeycomb that the ratio between the strain rate of the cell wall material and the nominal strain rate was between 1 and 2 [45]. The plateau stresses of MM-I with $c = 0$, $c = 0.02$ and $c = 0.06$ were calculated using Equation (5) and the results are shown in Figure 16(a). The full and dotted lines in Figure 16(a) are sequentially for one- and two-time increase in local strain rate. As shown in the same figure with a dotted-line box, the strain rate is effective in increasing the plateau stress up to relatively low velocities

(up to $\sim$30 m s^{-1}). At higher velocities, the plateau stress is nearly constant for $c = 0.02$ and slightly increases with velocity for $c = 0.06$. This is also well accord with the previous works on Al honeycomb and foam structures [29,34,35]. It is also noted that doubling the local strain rate results in comparatively low stress rise in the strain rate hardening models. The increased distal-end initial peak-stress of MM-I and MM-II from quasi-static until 20 m s^{-1} is therefore concluded to be likely due to the micro-inertia since both MM-I and M-II are strain rate insensitive. While, the increased distal-end initial peak-stress of MM-III and MM-IV from quasi-static until 20 m s^{-1} is due to both micro-inertia and strain rate. The experimental increase of distal-end initial peak-stress of the investigated corrugate structure within the same velocity range was also reported in another study [41]. The relative contributions of the effects to the dynamic distal-end peak-stress of the corrugated structure (MM-IV and 250 m s^{-1}) are shown in Figure 16(b). The contribution of quasi-static initial peak-stress, micro-inertia, strain hardening and strain rate for a relatively high strain rate sensitive alloy ($c = 0.06$) is sequentially 44, 12, 19 and 35%, respectively. For a relatively low strain rate sensitive alloy ($c = 0.02$), the contribution of strain rate decreases to 12% and the contribution of quasi-static initial peak-stress, micro-inertia and strain hardening increases sequentially to 52%, 14% and 22%. The effect of imperfect layer on the dynamic distal-end initial peak-stress is also noted relatively low, 5–7%. These results also confirmed the negligible effect of velocity on the distal-end initial peak-stresses of such cellular structures made of low strain rate hardening metals such as Al alloy investigated in this study.

5. Conclusions

The effect of the sets of material parameters of the Johnson and Cook flow stress model on the dynamic distal-end initial peak-stress and impact-end stress of a layered 1050 H14 aluminium corrugated structure was investigated numerically at quasi-static (0.0048 m s^{-1}) and dynamic (20, 60, 150 and 250 m s^{-1}) velocities. In the numerical and experimental direct impact tests, the corrugated sample was placed at the end of the incident bar of an SHPB set-up and an aluminium striker impinged the corrugated sample. The increase of striker velocity increased the impact-end stress, while the impact-end stress analysis showed a quasi-static homogenous mode at 0.0048 and 20 m s^{-1}, a transition mode at 60 m s^{-1} and a shock mode at 150 and 250 m s^{-1}. The stress calculations of the r-p-p-l model confirmed the shock mode of deformation at 150 and 250 m s^{-1}. A simple plateau stress analysis based on open-celled foam structure revealed the rapid increase of plateau stress up to $\sim$30 m s^{-1} in strain rate hardening models. At higher velocities, the plateau stress was nearly constant when $c = 0.02$ and slightly increased with increasing velocity when $c = 0.06$. Numerical results showed that the increase of velocity from quasi-static to 20 m s^{-1} increased the distal-end initial peak-stress, while it almost remained constant between 20 and 250 m s^{-1} for

all material models investigated. The increased distal-end initial peak-stress in MM-I and MM-II from quasi-static to $20 \, \text{m s}^{-1}$ was ascribed to the micro-inertia as both models were strain rate insensitive, while the increased distal-end initial peak-stress of MM-III and MM-IV from quasi-static until $20 \, \text{m s}^{-1}$ was ascribed to both micro-inertia and strain rate. The increase of distal-end initial peak-stress within the same velocity range was also previously noted in the tested corrugate structure. The numerical models showed almost no effect of the used sets of material model parameters on the impact-end stresses in the shock mode of deformation. The contribution of strain rate on the distal-end initial peak-stress was calculated relatively low as compared with that of strain hardening and micro-inertia for low strain rate hardening Al alloys. In designing the engineering components with the cellular structures made of low strain rate sensitive alloys against impact, the micro-inertia should be included in the homogenized geometrical models, simply by conducting tests at different velocities. The shock stress development in these structures can also be predicted by using simple material models at a specific velocity.

Disclosure statement

Acknowledgements

References

[1] Sun YL, Li QM. Dynamic compressive behaviour of cellular materials: A review of phenomenon, mechanism and modelling. Int J Impact Eng. 2018;112:74–115.

[2] Deshpande VS, Fleck NA. High strain rate compressive behaviour of aluminium alloy foams. Int J Impact Eng. 2000;24(3): 277–298.

[3] Sadot O, Ram O, Anteby I, et al. The trapped gas effect on the dynamic compressive strength of light aluminum foams. Mater Sci Eng A. 2016;659:278–286.

[4] Alvandi-Tabrizi Y, Whisler DA, Kim H, et al. High strain rate behavior of composite metal foams. Mater Sci Eng A–Struct Mater Properties Microstruct Process. 2015;631:248–257.

[5] Jung A, Pullen AD, Proud WG. Strain-rate effects in Ni/Al composite metal foams from quasi-static to low-velocity impact behaviour. Compos Part A–Appl Sci Manufact. 2016;85:1–11.

[6] Tam LL, Calladine CR. Inertia and strain-rate effects in a simple plate-structure under impact loading. Int J Impact Eng. 1991;11(3):349–377.

[7] Calladine CR, English RW. Strain-rate and inertia effects in the collapse of 2 types of energy-absorbing structure. Int J Mech Sci. 1984;26(11–12):689.

[8] Langseth M, Hopperstad OS. Static and dynamic axial crushing of square thin-walled aluminium extrusions. Int J Impact Eng. 1996;18(7–8):949–968.

[9] Paul A, Ramamurty U. Strain rate sensitivity of a closed-cell aluminum foam. Mater Sci Eng A. 2000;281(1–2):1–7.

[10] Zhao H, Elnasri I, Abdennadher S. An experimental study on the behaviour under impact loading of metallic cellular materials. Int J Mech Sci. 2005;47(4–5):757–774.

[11] Tagarielli VL, Deshpande VS, Fleck NA. The high strain rate response of PVC foams and end-grain balsa wood. Compos Part B-Eng. 2008;39(1):83–91.

[12] Barnes AT, Ravi-Chandar K, Kyriakides S, et al. Dynamic crushing of aluminum foams: part I – experiments. Int J Solids Struct. 2014;51(9):1631–1645.

[13] Tan PJ, Reid SR, Harrigan JJ, et al. Dynamic compressive strength properties of aluminium foams. Part I – experimental data and observations. J Mech Phys Solids. 2005;53(10): 2174–2205.

[14] Zou Z, Reid SR, Tan PJ, et al. Dynamic crushing of honeycombs and features of shock fronts. Int J Impact Eng. 2009; 36(1):165–176.

[15] Tan PJ, Reid SR, Harrigan JJ. On the dynamic mechanical properties of open-cell metal foams – a re-assessment of the 'simple-shock theory'. Int J Solids Struct. 2012;49(19–20): 2744–2753.

[16] Gaitanaros S, Kyriakides S. Dynamic crushing of aluminum foams: Part II – analysis. Int J Solids Struct. 2014;51(9): 1646–1661.

[17] Reid SR, Peng C. Dynamic uniaxial crushing of wood. Int J Impact Eng.. 1997;19(5–6):531–570.

[18] Harrigan JJ, Reid SR, Tan PJ, et al. High rate crushing of wood along the grain. Int J Mech Sci. 2005;47(4–5):521–544.

[19] Chen A, Kim H, Asaro RJ, et al. Non-explosive simulated blast loading of balsa core sandwich composite beams. Compos Struct. 2011;93(11):2768–2784.

[20] Wang S, Ding Y, Wang C, et al. Dynamic material parameters of closed-cell foams under high-velocity impact. Int J Impact Eng.. 2017;99:111–121.

[21] Liu H, Zhang Z, Liu H, et al. Theoretical investigation on impact resistance and energy absorption of foams with nonlinearly varying density. Compos Part B Eng. 2017; 116 :76–88.

[22] Zhang B, Lin Y, Li S, et al. Quasi-static and high strain rates compressive behavior of aluminum matrix syntactic foams. Compos Part B Eng. 2016;98:288–296.

[23] Liu H, Zhang Z, Liu H, et al. Effect of elastic target on Taylor–Hopkinson impact of low-density foam material. Int J Impact Eng.. 2016;94:109–119.

[24] Lopatnikov SL, Gama BA, Jahirul Haque M, et al. Dynamics of metal foam deformation during Taylor cylinder-Hopkinson bar impact experiment. Compos Struct. 2003;61(1–2):61–71.

[25] Elnasri I, Pattofatto S, Zhao H, et al. Shock enhancement of cellular structures under impact loading: Part I experiments. J Mech Phys Solids. 2007;55(12):2652–2671.

[26] Liu H, Cao ZK, Yao GC, et al. Performance of aluminum foam–steel panel sandwich composites subjected to blast loading. Mater Des. 2013;47(0):483–488.

[27] Odac IK, Güden M, Kılıçaslan C, Taşdemirci A. The varying densification strain in a multi-layer aluminum corrugate structure: direct impact testing and layer-wise numerical modelling. Int J Impact Eng. 2017;103:64–75.

[28] Tan PJ, Reid SR, Harrigan JJ, et al. Dynamic compressive strength properties of aluminium foams. Part II – 'shock' theory and comparison with experimental data and numerical models. J Mech Phys Solids. 2005;53(10):2206–2230.

[29] Wang P, Xu S, Li Z, et al. Experimental investigation on the strain-rate effect and inertia effect of closed-cell aluminum foam subjected to dynamic loading. Mater Sci Eng A. 2015;620: 253–261.

[30] Radford DD, Deshpande VS, Fleck NA. The use of metal foam projectiles to simulate shock loading on a structure. Int J Impact Eng. 2005;31(9):1152–1171.

[31] Kilicaslan C, Odaci IK, Gueden M. Single- and double-layer aluminum corrugated core sandwiches under quasi-static and dynamic loadings. J Sandwich Struct Mater. 2016;18(6): 667–692.

[32] Zhao H, Gary G. Crushing behaviour of aluminium honeycombs under impact loading. Int J Impact Eng. 1998;21(10): 827–836.

[33] Qiao JX, Chen CQ. In-plane crushing of a hierarchical honeycomb. Int J Solids Struct. 2016;85–86:57–66.

[34] Tao Y, Chen M, Chen H, et al. Strain rate effect on the out-of-plane dynamic compressive behavior of metallic honeycombs: experiment and theory. Compos Struct. 2015;132:644–651.

[35] Tao Y, Chen M, Pei Y, et al. Strain rate effect on mechanical behavior of metallic honeycombs under out-of-plane dynamic compression. J Appl Mech-Trans Asme. 2015;82(2):6.

[36] Kilicaslan C, Güdenİsmet M, Odacı IK, Taşdemirci A.. The impact responses and the finite element modeling of layered trapezoidal corrugated aluminum core and aluminum sheet interlayer sandwich structures. Mater Des. 2013;46:121–133.

[37] Kilicaslan C, Güdenİsmet M, Odacı IK, Taşdemirci A. Experimental and numerical studies on the quasi-static and dynamic crushing responses of multi-layer trapezoidal aluminum corrugated sandwiches. Thin-Walled Struct. 2014;78:70–78.

[38] Liu YD, Yu JL, Zheng ZJ, et al. A numerical study on the rate sensitivity of cellular metals. Int J Solids Struct. 2009;46(22–23): 3988–3998.

[39] Kilicaslan C, Odacı İK, Taşdemirci A, Güden M.. Experimental testing and full and homogenized numerical models of the low velocity and dynamic deformation of the trapezoidal aluminium corrugated core sandwich. Strain. 2014;50(3):236–249.

[40] Sarikaya M, Tasdemirci A, Guden M. Impact loading and modelling a multilayer aluminium corrugated/fin core: the effect of the insertion of imperfect fin layers. Strain. 2019;55(1):17.

[41] Sankaya M, Tasdemirci A, Guden M. Dynamic crushing behavior of a multilayer thin-walled aluminum corrugated core: the effect of velocity and imperfection. Thin-Walled Struct. 2018; 132:332–349.

[42] Lindholm US, Bessey RL, Gv S. Effect of strain rate on yield strength, tensile strength and elongation of three aluminium alloys. J Mater JMLSA. 1971;6:119.

[43] Harrigan JJ, Reid SR, Yaghoubi AS. The correct analysis of shocks in a cellular material. Int J Impact Eng.. 2010;37(8): 918–927.

[44] Ashby MF, Medalist RFM. The mechanical-properties of cellular solids. MTA. 1983;14(9):1755–1769.

[45] Zhao H, Elnasri I, Li HJ. The mechanism of strength enhancement under impact loading of cellular materials. Adv Eng Mater. 2006;8(9):877–883.